THE JOURNAL OF BIOLOGICAL CHEMISTRY VOL. 286, NO. 50, pp. 43515–43526, December 16, 2011

Mimicry of the Regulatory Role of Urokinase in Lamellipodia Formation by Introduction of a Non-native Interdomain Disulfide Bond in Its Receptor*[S]

Received for publication, September 2, 2011, and in revised form, October 13, 2011 Published, JBC Papers in Press, October 24, 2011, DOI 10.1074/jbc.M111.300020

Henrik Gårdsvoll[‡§], Magnus Kjaergaard[¶], Benedikte Jacobsen[‡§], Mette C. Kriegbaum[‡], Mingdong Huang[§‖], and Michael Ploug[‡§1]

From the [‡]Finsen Laboratory, Rigshospitalet & Biotech Research and Innovation Centre (BRIC), Copenhagen Biocenter, Ole Maaløes Vej 5, DK-2200 Copenhagen N, Denmark, [§]Danish-Chinese Centre for Proteases and Cancer, the [¶]Department of Biology, University of Copenhagen, Ole Maaløes Vej 5, DK-2200, Copenhagen N, Denmark, and the [‖]State Key Laboratory of Structural Chemistry, Fujian Institute of Research on the Structure of Matter, Chinese Academy of Sciences, Fuzhou, Fujian 350002, China

Background: The urokinase receptor (uPAR) acts as a modulator of lamellipodia formation on vitronectin-rich matrices.
Results: Constraining the flexibility of uPAR by an interdomain cross-link drives it into a constitutively active state.
Conclusion: Conformational dynamics of uPAR is important for its function and is regulated by uPA binding.
Significance: This flexibility needs to be considered when investigating and targeting the function of uPAR.

The high-affinity interaction between the urokinase-type plasminogen activator (uPA) and its glycolipid-anchored receptor (uPAR) plays a regulatory role for both extravascular fibrinolysis and uPAR-mediated adhesion and migration on vitronectin-coated surfaces. We have recently proposed that the adhesive function of uPAR is allosterically regulated via a "tightening" of its three-domain structure elicited by uPA binding. To challenge this proposition, we redesigned the uPAR structure to limit its inherent conformational flexibility by covalently tethering domains DI and DIII via a non-natural interdomain disulfide bond ($uPAR^{H47C\text{-}N259C}$). The corresponding soluble receptor has 1) a smaller hydrodynamic volume, 2) a higher content of secondary structure, and 3) unaltered binding kinetics towards uPA. Most importantly, the purified $uPAR^{H47C\text{-}N259C}$ also displays a gain in affinity for the somatomedin B domain of vitronectin compared with $uPAR^{wt}$, thus recapitulating the improved affinity that accompanies uPA-$uPAR^{wt}$ complex formation. This functional mimicry is, intriguingly, operational also in a cellular setting, where it controls lamellipodia formation in uPAR-transfected HEK293 cells adhering to vitronectin. In this respect, the engineered constraint in $uPAR^{H47C\text{-}N259C}$ thus bypasses the regulatory role of uPA binding, resulting in a constitutively active uPAR. In conclusion, our data argue for a biological relevance of the interdomain dynamics of the glycolipid-anchored uPAR on the cell surface.

The glycolipid-anchored urokinase-type plasminogen activator receptor (uPAR)[2] (1) is *the* single membrane protein responsible for focalizing urokinase-mediated plasminogen activation to cell surfaces both *in vitro* and *in vivo* (2–4). This is accomplished through a high-affinity interaction ($K_D \sim 0.5$ nM) between uPAR and the N-terminal growth factor-like domain (GFD) of the urokinase-type plasminogen activator (uPA). Genetic abrogation of this bimolecular assembly *in vivo* by either wholesale gene ablations of the corresponding *Plaur* or *Plau* genes or by selectively abrogating the uPA-uPAR interaction *sensu stricto*, through redesigning the *Plau* gene to encode a uPA protein with a nonfunctional β-hairpin, all lead to pathological hepatic fibrin depositions associated with chronic inflammation (5, 6). These genetic dissections clearly emphasize a role for the uPA-uPAR axis in maintenance of extravascular fibrin homeostasis under normal physiological conditions. As both uPAR and uPA are expressed by either tumor or stromal cells in the invasive microenvironment of many human cancers, including colon (7), breast (8), and pancreatic (9) carcinomas, this enzyme system is also assumed to contribute to the pathogenesis of these diseases. Elevated levels of uPA and uPAR are accordingly important biomarkers of poor prognosis for such patients (10, 11), and both are considered attractive targets for drug development (12, 13).

Although uPA undisputedly is the *bona fide* protease ligand for uPAR, this receptor also cooperates with other proteins that are involved in cell adhesion and migration, *e.g.* vitronectin and certain integrins (14–18). The direct interactions between uPAR, uPA, and vitronectin have recently been thoroughly characterized both biochemically and structurally. Complementary functional epitopes on uPAR and its biological ligands (uPA and vitronectin) have been

* This work was supported by grants from The Danish National Research Foundation (Centre for Proteases and Cancer) and The Lundbeck Foundation.
[S] The on-line version of this article (available at http://www.jbc.org) contains supplemental Table S1 and Figs. S1–S3.
[1] To whom correspondence should be addressed: Finsen Laboratory, Rigshospitalet/BRIC, Copenhagen Biocenter, Rm. 3.3.31, Ole Maaløes Vej 5, DK-2200 Copenhagen N, Denmark. Fax: 45-35453797; E-mail: m-ploug@finsenlab.dk.

[2] The abbreviations used are: uPAR, urokinase-type plasminogen activator receptor; uPA, urokinase-type plasminogen activator; ATF, amino-terminal fragment of uPA; GFD, growth factor-like domain; LU domains, Ly6/uPAR-like domains; SMB, somatomedin B-like domain of vitronectin; ANS, 8-Anilino-1-naphthalene sulfonate; DI, DII, DIII, domain I, II, and III; chym, chymotrypsin.

identified by systematic alanine scanning mutagenesis (5, 17, 19, 20), and the corresponding binding interfaces are well defined at high resolution by x-ray crystallography (5, 21, 22). The proposed molecular interplay between uPAR and integrins remains, however, to be defined at the structural level (15).

From extensive biochemical and structural studies, it is now clear that all three Ly6/uPAR/α-neurotoxin-like (LU) domains in uPAR cooperate to assemble the composite binding sites for both uPA and vitronectin, which encompass distinct surface-exposed interdomain junctions on the receptor (13, 23). Recently, we introduced a molecular model for uPAR function, which assumes that uPAR may explore different conformational states having distinct functional properties (24). According to this model, unoccupied human uPAR predominantly exists in an *open* conformation, which does not support uPAR-dependent induction of lamellipodia on vitronectin-coated surfaces. This model implies that ligand binding to the GFD of uPA shifts the conformational equilibrium in uPAR towards a more *closed* conformation, which renders uPAR active in supporting lamellipodia formation (24).

Based on the crystal structures available for uPAR in complex with the amino-terminal fragment (ATF) of uPA (5, 21) and a high-affinity antagonist peptide (25), we have now designed a stabilized uPAR variant, which cannot populate the allegedly *open* native conformation due to the constraint introduced by an engineered interdomain disulfide bond between uPAR domains I and III (DI and DIII). Whereas maintaining unaltered binding kinetics towards uPA, this engineered receptor gains a number of new functional properties due to this constrained conformation. Most importantly, we found that this particular receptor is constitutively active in stimulating lamellipodia formation on vitronectin-rich matrices in the absence of uPA under conditions where the corresponding unconstrained uPAR is unable to do so. Besides emphasizing the predictive power of our molecular model for uPAR function (24), this study also opens new avenues for crystallizing the unoccupied receptor,[3] the structure of which has so far proven elusive. Finally, this constrained uPAR mutant maintains unaltered binding kinetics towards uPA even after cleavage of the protease-sensitive linker region between DI and DII, which consequently offers the unique possibility of studying the functional consequences of this cleavage *per se*, without facing confounding effects from subsequent interdomain dissociations and release of DI as is the case for the wild-type protein (27–29).

MATERIALS AND METHODS

Chemicals and Protein Reagents—Human pro-uPA$^{1-411}$ and ATF$^{1-143}$ were expressed by *Drosophila melanogaster* S2 cells and affinity purified as described previously (19). The growth factor-like domain of human uPA (GFD$^{1-48}$) was a kind gift from S. Rosenberg (30). A His-tagged SMB$^{1-47}$ domain from human vitronectin was expressed in *Pichia pastoris* and purified as described (31). TLCK-treated chymotrypsin was from Worthington (Freehold, NJ) and was stored at −80 °C as 1 mg/ml stock solutions in 1 mM HCl. Monoclonal anti-uPAR antibodies were produced in-house (R2, R3, R5, R8, R9, R21, and mR1), purchased from Acris Antibodies, Herford Cambridge, UK (VIM-5), or kindly supplied by Dr. U. Weidle, Roche Applied Science (H2).

Expression, Purification, and Chymotrypsin Cleavage of Soluble Human uPAR Mutants—Soluble forms of human uPAR$^{1-283}$ were expressed by stably transfected *D. melanogaster* S2 cells as described previously (32). The secreted proteins were purified from the culture medium by a peptide-based, one-step affinity chromatography for uPAR^{wt} (33) and by immunoaffinity chromatography using the monoclonal anti-uPAR antibody R2 for the new uPAR$^{H47C\text{-}N259C}$ and uPAR$^{K50C\text{-}D254C}$ mutants.

Chymotrypsin treatment of the purified recombinant uPAR variants was performed essentially as described (34) using conditions delimiting the cleavage to the single peptide bond between Tyr^{87}-Ser^{88}. This specificity was accomplished by incubating purified uPAR with chymotrypsin at a ratio of 5000:1 (w/w) for 12 h at room temperature.

Size Exclusion Chromatography—Recombinant and affinity-purified uPAR^{wt}, uPAR$^{H47C\text{-}N259C}$, and uPAR$^{H47C\text{-}N259C/chym}$ were subjected to size exclusion chromatography using a Superdex^{TM} 200 (10/300) column operated at 1 ml/min by an Äktapurifier^{TM} HPLC system. The column was equilibrated with 20 mM sodium phosphate buffer, pH 7.2, 50 mM Na_2SO_4, and calibrated with the appropriate molecular mass markers (ribonuclease (13,700 Da), carbonic anhydrase (29,000 Da), ovalbumin (43,000 Da), and conalbumin (75,000 Da)). Sample volumes of 200 μl containing 3 mg/ml of the respective recombinant uPAR mutants were applied and analyzed at room temperature.

Circular Dichroism Spectroscopy—Far UV circular dichroism (CD) spectra were recorded in a 1-mm quartz cuvette using a Jasco J-810 equipped with a PTC-4233 Peltier temperature controller. The spectra were acquired at 20 °C from 250 to 190 nm with a scan speed of 20 nm/min and a response time of 1 s averaging 40 scans for each measurement. All measurements were performed in 20 mM sodium phosphate buffer, pH 7.2, 50 mM Na_2SO_4, and a protein concentration of 3 μM. Protein samples were purified and monomer status was ensured by gel filtration prior to CD analysis.

ANS Fluorescence Measurements—8-Anilino-1-naphthalene sulfonate (ANS) fluorescence was recorded using a PerkinElmer LS50B fluorimeter using a 5-mm square cuvette. The fluorophore was excited at 370 nm, and the fluorescence emission was measured from 400 to 600 nm using slit widths of 5 nm. Measurements were performed in the same buffer as CD analysis using a protein concentration of 5 μM and an ANS concentration of 10 μM. GFD was added from a concentrated stock to a final concentration of 15 μM, resulting in a 2.5% dilution.

Surface Plasmon Resonance Studies—Real time interaction studies were carried out on Biacore 3000^{TM} or T200^{TM} instruments (Biacore, Uppsala, Sweden) using 10 mM HEPES, 150 mM

[3] X. Xu, H. Gårdsvoll, C. Yuan, L. Lin, M. Ploug, and M. Huang, submitted for publication.

NaCl, 3 mM EDTA, supplemented with either 0.005 or 0.05% (v/v) surfactant P-20 at pH 7.4 as running buffer. For kinetic evaluations, soluble uPAR (0.1 μg/ml) was immobilized covalently on a carboxymethylated dextran matrix (CM5 sensor chip) using *N*-hydroxysuccinimide/*N*-ethyl-*N*′-(3-(diethylamino)propyl)-carbodiimide yielding coupling levels of ~200 RU, ~6 fmol/mm^2. To obtain comparable measurements for uPAR^{wt}, uPAR$^{H47C\text{-}N259C}$, and uPAR$^{H47C\text{-}N259C/chym}$, they were immobilized to similar densities in parallel flow cells. Kinetic rate constants for these uPA-uPAR interactions were determined from the analyses of serial 2-fold dilutions covering 0.1–50 nM of the various uPA derivatives (GFD, ATF, and pro-uPA) at a flow rate of 50 μl/min at 20 °C. After each run the sensor chip was regenerated by two consecutive injections of 0.1 M acetic acid in 0.5 M NaCl. The kinetic rate constants, k_{on} and k_{off}, were derived from these real-time interaction analyses by fitting the association and dissociation phases to a bimolecular interaction model using BIAevaluation 4.1 software (Biacore, Uppsala, Sweden), as described in detail previously (19). Thermodynamics of the uPA-uPAR interaction were assessed by coupling pro-uPA onto the sensor chip and measuring the interaction with 2-fold dilution series covering 3–50 nM uPAR^{wt}, uPAR$^{H47C\text{-}N259C}$, and uPAR$^{H47C\text{-}N259C/chym}$ at 6 different temperatures covering 5–37 °C at 50 μl/min by a Biacore T200 instrument. Entropy ($\Delta S°$), enthalpy ($\Delta H°$), and heat capacity ($\Delta C_p°$) changes were derived from nonlinear van't Hoff plots using the evaluation software (version 1.0) supplied with the equipment (supplemental Fig. S1).

Inducible Expression of Glycolipid-anchored uPAR Mutants in HEK293 Cells—The uPAR mutants were stably expressed in HEK293 cells by the Flp-In T-Rex system from Invitrogen: uPAR^{wt}, uPAR^{W32A}, uPAR^{R91D}, and uPAR$^{W32A\text{-}R91D}$. The corresponding four mutants were also expressed in the context of the disulfide-constrained receptor uPAR$^{H47C\text{-}N259C}$, *i.e.* uPAR$^{H47C\text{-}N259C/W32A}$, uPAR$^{H47C\text{-}N259C/R91D}$, and uPAR$^{H47C\text{-}N259C/W32A\text{-}R91D}$.

Construction of the expression vector pcDNA5/FRT/TO/uPAR encoding full-length uPAR^{wt} has previously been described (18). Mutant constructs were generated by introducing the corresponding mutations into this vector with the QuikChange Multi Site-directed Mutagenesis kit (Stratagene, AH Diagnostics, Aarhus). The parental Flp-In T-Rex-293 cell line was grown in minimal essential medium supplemented with Earle's and GlutaMAX I (Invitrogen 41090–028) plus nonessential amino acids, 10% (v/v) FCS, 100 units/ml of penicillin, 100 μg/ml of streptomycin with the addition of 15 μg/ml of blasticidin S and 100 μg/ml of Zeocin at 37 °C in a 5% CO_2 humidified incubator. Stable, tetracycline-inducible cell lines were generated by co-transfection with pcDNA5/FRT/TO expression vectors and pOG44 in a 1:10 ratio using Lipofectamine 2000 as transfection agent followed by selection in medium as above omitting Zeocin, but adding 150 μg/ml of hygromycin B. Expression of uPAR was induced by adding 1 μg/ml of tetracycline to the medium.

Determining uPAR Expression Levels and Affinities of Transfected HEK293 Cells—To compare the uPAR expression levels in the various transfected HEK293 cell lines, these were cultured in the presence of 1 μg/ml of tetracycline. Cells were harvested using a rubber policeman, washed in PBS, and

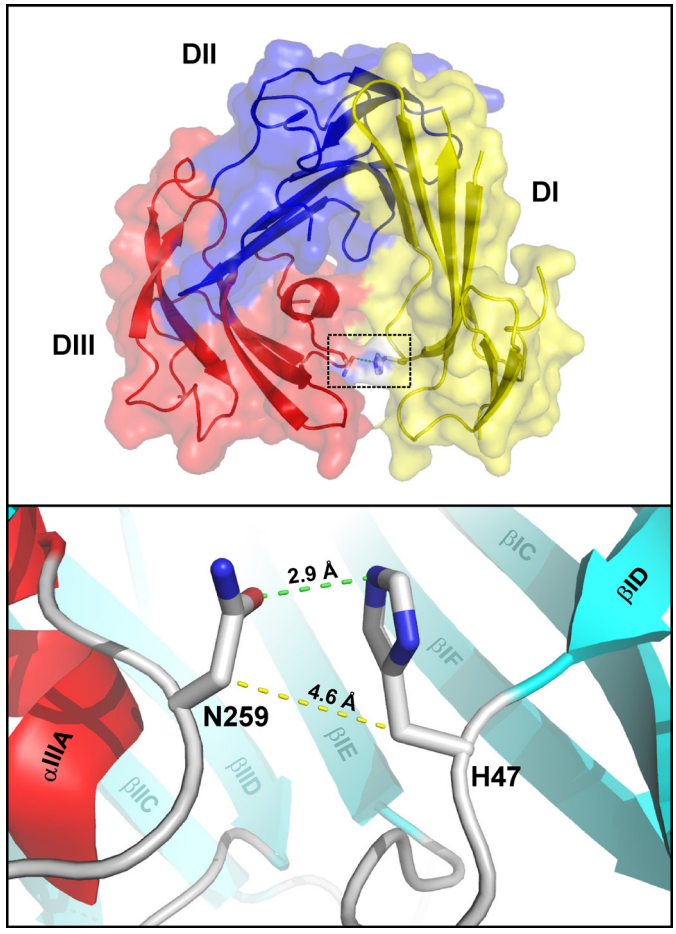

FIGURE 1. **Interdomain interface between DI and DIII in human uPAR.** The structure of the ligand-induced closed conformation of the modular human uPAR is shown in the *upper panel* as a combined ribbon and semitransparent surface representation. The three LU domains are highlighted by color coding: DI (*yellow*), DII (*blue*), and DIII (*red*). The bound ATF is omitted for clarity and the large hydrophobic uPA-binding cavity is facing the observer. The interdomain hydrogen bonding between His^{47} and Asn^{259} is highlighted by the *hatched box*. The *lower panel* shows a close up of this region (rotated 90°), where the distance between the two C_β-carbon atoms is shown as a *dotted yellow line* (4.6 Å). The nomenclature of the secondary structures shown follows previously established guidelines for proteins with multiple LU domains (5, 25), and the PDB 2FD6 coordinates were used for generating these illustrations.

counted in a NucleoCounter™. The cell pellet was collected by centrifugation and lysed in 500 μl of 1.5% (v/v) Triton X-100, 0.1 M Tris, pH 8.1, 10 mM EDTA, 10 μg/ml of Trasylol, and 1 mM phenylmethylsulfonyl fluoride at a cell density of 1–2 × 10^7 cells/ml. The uPAR contents in these lysates were determined by a specific ELISA (35).

To assess the uPA-binding capacity and affinity of the transfected HEK293 cell lines, these were seeded (6 × 10^5 cells/well) in 24-well plates and allowed to adhere for 2–3 days in the presence of 1 μg/ml of tetracycline, reaching confluence before being subjected to a solid-phase uPA binding assay. In brief, the adherent cells were incubated with 3-fold dilution series of Eu^{3+}-labeled pro-uPA (0.05–300 nM pro-uPA with a labeling density of 2.0 Eu/uPA) in 400 μl of minimal essential medium with 10% (v/v) FCS for 24 h at 4 °C. After extensive washings, the number of adherent cells in representative wells was counted in a NucleoCounter after detachment by trypsin/

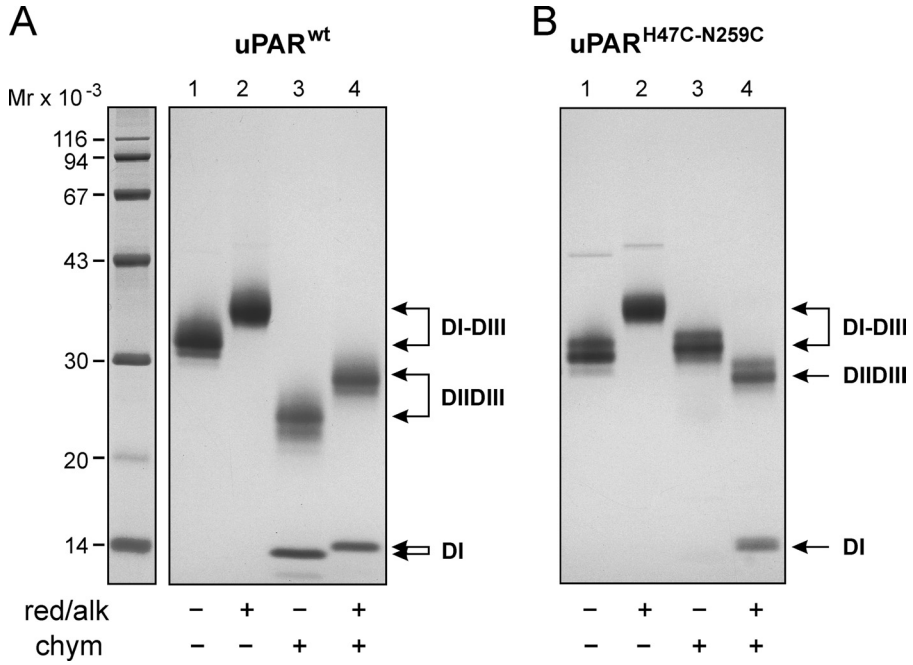

FIGURE 2. **Introduction of a disulfide between DI and DIII in uPAR$^{H47C-N259C}$.** Analysis of recombinant wild-type human uPAR$^{1-283}$ by SDS-PAGE followed by Coomassie staining is shown in *panel A*. Intact uPAR is analyzed before (*lane 1*) and after reduction of its disulfide bonds (*lane 2*). Specific interdomain cleavage of the linker region between DI and DII accomplished by limited chymotrypsin cleavage after Tyr^{87} (26) releasing DI$^{1-87}$, which is detected along with DIIDIII$^{88-283}$ by SDS-PAGE without prior reduction of disulfide bonds (compare *lanes 3* and *4*). Analysis of the disulfide-constrained uPAR$^{H47C-N259C}$ followed the same strategy illustrated in *panel B*. Release of DI$^{1-87}$ in this mutant requires both cleavage after Tyr^{87} by chymotrypsin *and* subsequent reduction of the disulfide bonds (compare *lanes 3* and *4*). These experiments show that the two non-native cysteines introduced in the domain interface between DI and DIII spontaneously oxidize to a very high yield during protein expression and secretion.

EDTA treatment for 1–2 min at 37 °C. For quantification of pro-uPA binding, the adherent cells were lysed for 5 min in 400 μl of PBS containing 0.125% (v/v) Triton X-100. After centrifugation for 10 min at 4 °C (10,000 × *g*), the supernatants were diluted 5 times in DELFIA^{TM} enhancement solution, and the bound uPA was quantified by time-resolved fluorescence using a Fluostar Optima fluorometer (PerkinElmer Life Sciences) with excitation set at 340 nm and reading emission at 615 nm with a 400-μs delay and a 400-μs acquisition window. Nonspecific binding was assessed by a parallel measurement of Eu-labeled pro-uPA binding to the corresponding cell lines without prior tetracycline induction of uPAR expression.

Lamellipodia Formation on Vitronectin-coated Coverslips—The functional impacts of the above mentioned mutations in glycolipid-anchored uPAR on cellular responses upon vitronectin exposure were measured as described previously (16, 24). In brief, transfected HEK293 cells were seeded on vitronectin-coated glass coverslips for 24 h allowing their attachment to the matrix, and this was followed by an additional incubation for 24 h after exchange to fresh medium, which in some cases contained additives such as mAbs or uPA derivatives. To facilitate examination of lamellipodia formation, the adherent cells were fixed on the coverslips, permeabilized, and stained with Alexa 488-conjugated phalloidin to visualize actin filaments. Finally, the extent of lamellipodia formation was evaluated using the previously described quantitative protrusion index (24), providing a score ranging from 0 to 24 for each determination.

Miscellaneous—All graphic artwork on protein structures were generated by PyMol (Schrödinger, Portland, OR). Protein masses were determined by matrix-assisted laser desorption mass spectrometry (Autoflex II^{TM} MALDI-TOF/TOF, Bruker Daltonics GmbH, Bremen, Germany) after deposition in sinapinic acid.

RESULTS

Rational Design of an Interdomain Disulfide Cross-link in Human uPAR—The formation of a functional high-affinity binding cavity for the growth factor-like domain of uPA requires the modular assembly of all three LU domains in the glycolipid-anchored uPAR (36). Nonetheless, we have recently proposed a model for the role of uPAR in vitronectin-dependent cell adhesion and migration, where unoccupied uPAR predominantly exists in an *open* inactive conformation (24). According to this proposition, the mere occupancy of the hydrophobic cavity in uPAR by the β-hairpin in GFD induces the formation of a more *closed* and compact receptor conformation, which exhibits an increased activity in inducing lamellipodia on cells plated on vitronectin-rich matrices. One important ramification of this model, which emphasizes the importance of the conformational dynamics of uPAR for its function, is the prediction that constraining the interdomain mobility in uPAR by introduction of a covalent cross-link in the interdomain interface could potentially create a constitutively active receptor. Inspired by this intriguing possibility, we searched the interface between uPAR DI and DIII for optimal distances and geometries, which could permit the formation of a stable disulfide bond, *i.e.* with an optimal distance between the C_β-atoms of 5.6 Å (37). Search in three different crystal structures of uPAR-ATF complexes (Protein Data Bank codes 2FD6, 2I9B, and 3BT1) identified two potential candidates, *i.e.*

His^{47}-Asn^{259} and Lys^{50}-Asp^{254}, both of which are involved in the formation of interdomain hydrogen bonding and having their C_β-atoms positioned 4.4–4.9 and 8.1–8.8 Å apart, respectively. The location of the more promising of these positions is illustrated in Fig. 1.

Engineering a Covalent Cross-link between DI and DIII in uPAR—To explore the aptness of these hydrogen-bonded residues as foci for new covalent interdomain cross-links, we introduced their pairwise replacement by cysteine residues and expressed the corresponding proteins $uPAR^{H47C\text{-}N259C}$ and $uPAR^{K50C\text{-}D254C}$ in *Drosophila* S2 cells. Although both mutant proteins are expressed well by this system and both produce high yields of pure protein after immunoaffinity chromatography, $uPAR^{H47C\text{-}N259C}$, nonetheless, proved far superior in its ability to oxidize the free thiol groups and thus form the desired interdomain covalent cross-link. This property is clearly demonstrated in Fig. 2, where the liberation of uPAR DI from the rest of the molecule requires cleavage of the linker region at Tyr^{87} by chymotrypsin *as well as* subsequent reduction of the protein disulfide bonds (*panel B*, *lanes 3* and *4*). This is in sharp contrast to $uPAR^{wt}$, where the mere cleavage of the linker region releases DI (34) without reduction of disulfide bonds, as illustrated in *panel A*, *lanes 3* and *4*. In all subsequent studies, we therefore focused on $uPAR^{H47C\text{-}N259C}$, as this mutant exhibits a remarkable inherent efficacy in forming this non-natural interdomain disulfide bond.

Physicochemical Properties of Purified $uPAR^{H47C\text{-}N259C}$—To further characterize the consequences of this interdomain cross-link on the physicochemical properties of uPAR, we subjected the purified $uPAR^{wt}$, $uPAR^{H47C\text{-}N259C}$, and $uPAR^{H47C\text{-}N259C/chym}$ produced in *Drosophila* S2 cells to size exclusion chromatography in 20 mM phosphate buffer, pH 7.2, including 50 mM Na_2SO_4 (compatible with subsequent CD analysis). As illustrated by the chromatograms shown in Fig. 3*A*, this experiment reveals a surprisingly large difference in the hydrodynamic volume of $uPAR^{wt}$ (eluting at 15.8 ml) compared with $uPAR^{H47C\text{-}N259C}$ (eluting at 16.2 ml). Identical elution profiles displaying similar differences in retention times were obtained if the experiment was repeated in 20 mM phosphate buffer, pH 7.2, including 150 mM NaCl (data not shown). The notable difference in elution profiles cannot be ascribed to dissimilar molecular masses of the two recombinant proteins caused by micro- and/or macroheterogeneity in the post-translational processing of *N*-linked glycosylation sites as the average masses recorded by MALDI-MS are almost identical, *i.e.* $uPAR^{wt}$ ~35.051 Da and $uPAR^{H47C\text{-}N259C}$ ~35.064 Da (data not shown). The most likely explanation for the differences in the hydrodynamic volumes is that $uPAR^{wt}$ adopts a more *open* and extended conformation with a larger Stokes radius compared with a more *closed* and compact conformation stabilized by the disulfide constraint in $uPAR^{H47C\text{-}N259C}$.

A distinct, but much smaller increase in the hydrodynamic volume of $uPAR^{H47C\text{-}N259C}$ is also observed after chymotrypsin cleavage of the Tyr^{87}-Ser^{88} peptide bond (eluting at 16.1 ml), which is located in the linker region connecting DI and DII (Fig. 3*A*). This experiment thus clearly shows that DI remains attached to DIIDIII in the cleaved $uPAR^{H47C\text{-}N259C}$ mutant, as opposed to $uPAR^{wt}$ treated identically (34), and that this cleav-

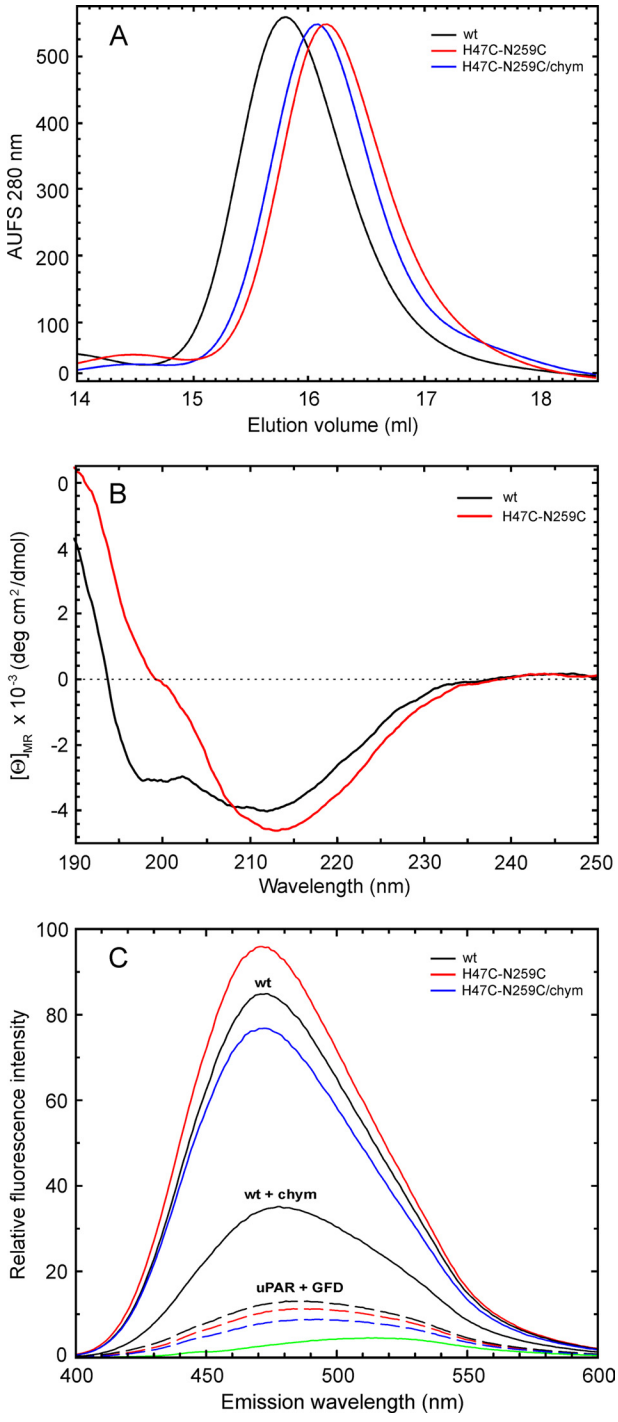

FIGURE 3. **Physicochemical properties of $uPAR^{H47C\text{-}N259C}$.** The hydrodynamic volumes of recombinant $uPAR^{wt}$ (*black*), $uPAR^{H47C\text{-}N259C}$ (*red*), and $uPAR^{H47C\text{-}N259C/chym}$ (*blue*) were compared by size exclusion chromatography on a Superdex 200 column (*panel A*). These elution profiles reveal that $uPAR^{wt}$ possesses a significantly larger hydrodynamic volume (M_r of 48.6×10^3) compared with both $uPAR^{H47C\text{-}N259C}$ (M_r of 41.5×10^3) and $uPAR^{H47C\text{-}N259C/chym}$ (M_r of 42.7×10^3), where the relative size estimates shown in *parentheses* are calculated relative to a mixture of globular protein standards analyzed in parallel. *Panel B* shows the far UV CD spectra of 3 μM purified $uPAR^{wt}$ (*black*) and $uPAR^{H47C\text{-}N259C}$ (*red*) in the same buffer as in *A*. *Panel C* shows the fluorescence emission spectra recorded for 5 μM $uPAR^{wt}$ (*black*), $uPAR^{H47C\text{-}N259C}$ (*red*), and $uPAR^{H47C\text{-}N259C/chym}$ (*blue*) in the presence of 10 μM ANS after excitation at 370 nm. The scans were repeated after addition of 15 μM GFD (*dotted lines*). The emission spectra for 15 μM GFD alone in 10 μM ANS is shown for comparison (*green*).

TABLE 1
Kinetic rate constants for the uPA-uPAR$^{H47C-N259C}$ interaction

Ligand[a]	Immobilized reactant[b]	k_{on}[c]	k_{off}[c]	K_d[c]	R_{max}[d]
		$10^5\ M^{-1}s^{-1}$	$10^{-4}\ s^{-1}$	$10^{-9}\ M$	*fmol/mm²*
Pro-uPA^{S356A}	uPAR^{wt}	7.89 ± 1.52	1.10 ± 0.13	0.14	1.7
Pro-uPA^{S356A}	uPAR$^{H47C-N259C}$	7.49 ± 1.34	0.67 ± 0.09	0.09	2.4
Pro-uPA^{S356A}	uPAR$^{H47C-N259C/chym}$	7.25 ± 1.08	0.56 ± 0.04	0.08	3.1
ATF$^{1-143}$	uPAR^{wt}	10.2 ± 2.18	1.06 ± 0.16	0.11	2.3
ATF$^{1-143}$	uPAR$^{H47C-N259C}$	9.91 ± 2.18	1.06 ± 0.19	0.12	2.2
ATF$^{1-143}$	uPAR$^{H47C-N259C/chym}$	9.86 ± 1.37	0.63 ± 0.23	0.07	3.2
GFD$^{1-48}$	uPAR^{wt}	4.23 ± 1.40	1.76 ± 0.25	0.48	2.2
GFD$^{1-48}$	uPAR$^{H47C-N259C}$	4.59 ± 1.68	1.65 ± 0.34	0.43	2.2
GFD$^{1-48}$	uPAR$^{H47C-N259C/chym}$	4.38 ± 1.86	1.02 ± 0.34	0.36	2.6

[a] Two-fold dilution series of ligands were measured at 20 °C at a flow rate of 50 μl/min covering the concentration range from 0.1 to 50 nM. Long dissociation phases (20 min) were included due to the tight binding of these ligands (supplemental Fig. S2).
[b] Low levels of uPAR were immobilized by amine chemistry in 3 consecutive flow cells of a CM5 sensor chip: uPAR^{wt} (306 RU), uPAR$^{H47C-N259C}$ (201 RU), and uPAR$^{H47C-N259C/chym}$ (221 RU). These levels correspond approximately to a surface density of 6–9 fmol/mm².
[c] The kinetic rate constants for the interaction between immobilized uPAR variants and the shown uPA derivatives were measured as specified under "Materials and Methods."
[d] R_{max} values were calculated from the Langmuir fitting assuming that 1 RU ~ 1 pg/mm². This shows that uPAR$^{H47C-N259C}$ retains a higher specific binding activity (40%) compared to uPAR^{wt} (24%) after covalent immobilization, which presumably reflects the increased protein stability of the constrained uPAR mutant.

age is accompanied by a minor increase in the hydrodynamic volume, which possibly indicates that the linker region now adopts a less confined conformation.

Comparison of the far UV CD spectra recorded for uPAR^{wt} and uPAR$^{H47C-N259C}$ demonstrates (Fig. 3*B*) that the covalent interdomain cross-link in uPAR$^{H47C-N259C}$ increases the average β-sheet content and decreases the random coil elements compared with the wild-type protein, as seen by the negative signals that increase at 213 nm and decrease at 200 nm. This finding is consistent with our recent proposition (24) that uPAR^{wt} exists in a dynamic equilibrium between an open and a closed form. In this model, the closed conformation is assembled by combining the individual β-strands of the 3 LU domains into a central 13-stranded interdomain β-sheet, which ultimately creates the hydrophobic uPA-binding cavity (21, 25).

To test if this hydrophobic ligand-binding cavity actually is preserved in the constrained uPAR$^{H47C-N259C}$, we subsequently measured the impact of the purified protein on the fluorescence emission spectrum of the external fluorophore ANS, which reports on the availability of an unoccupied and functional uPA binding site in uPAR (36). As evident from Fig. 3*C*, uPAR$^{H47C-N259C}$ is indeed able to enhance the quantum yield of ANS, which is accompanied by a large blue shift of the fluorescence emission maximum from 515 to 470 nm. Importantly, this enhanced fluorescence is abrogated upon saturation with GFD, demonstrating that a hydrophobic and functional uPA-binding cavity is correctly assembled in uPAR$^{H47C-N259C}$. Nonetheless, the ANS fluorescence of this mutant is essentially insensitive to chymotrypsin cleavage in the linker region between DI and DII leading to a reduction of only 20% in the intensity at 470 nm, which is relatively small compared with the 59% reduction observed for uPAR^{wt} (36). This suggests that the uPA binding site remains intact in uPAR$^{H47C-N259C/chym}$ despite cleavage of the Tyr^{87}-Ser^{88} peptide bond. This notion is further substantiated by the fact that the uPAR$^{H47C-N259C/chym}$-mediated enhancement of ANS fluorescence is completely abolished by the addition of a 3-fold molar excess of GFD (Fig. 3*C*).

Kinetic Rate Constants for the Interaction with uPA Are Not Altered in uPAR$^{H47C-N259C}$—To explore whether the covalent cross-link between uPAR DI and DIII has any impact on the binding kinetics to uPA, we immobilized low and comparable levels of uPAR^{wt} and uPAR$^{H47C-N259C}$ on a Biacore CM5 sensor chip and measured the binding kinetics of pro-uPA^{S356A}, ATF, and GFD in real-time. As shown in Table 1, there is no significant difference between uPAR^{wt} and uPAR$^{H47C-N259C}$ in the derived kinetic rate constants for their interactions with these uPA derivatives at 20 °C, further emphasizing that the integrity of the hydrophobic binding cavity is not perturbed by the non-natural covalent cross-link between DI and DIII. Although these equilibrium binding constants for uPA are remarkably similar (Table 1), they, nonetheless, represent a typical example of entropy-enthalpy compensation (38), as the uPA-uPAR$^{H47C-N259C}$ interaction presents a more favorable entropy contribution ($T\Delta S°$ of 7.2 kJ mol^{-1}) compared with the corresponding uPA-uPAR^{wt} interaction ($T\Delta S°$ of −5.5 kJ mol^{-1}), as illustrated in supplemental Fig. S1.

As the data in Fig. 3*C* reveal that the hydrophobic ligand-binding cavity in uPAR$^{H47C-N259C}$ is preserved after chymotrypsin cleavage in the linker region between DI and DII, we subsequently addressed whether this unexpected property also translates into unaltered uPA binding kinetics. To clarify this issue, we compared the kinetics of uPA binding to uPAR$^{H47C-N259C}$ and uPAR$^{H47C-N259C/chym}$ by surface plasmon resonance. Consistent with the ANS data, both proteins exhibit pairwise identical rate constants for their interactions with pro-uPA^{S356A}, ATF, and GFD (Table 1 and supplemental Fig. S2), further consolidating the unique maintenance of a functional and hydrophobic ligand-binding cavity after cleavage of the linker between DI and DII in uPAR$^{H47C-N259C}$. A similar scenario is clearly not applicable to uPAR^{wt}, where the progression of the enzymatic cleavage actually can be monitored in real-time by the concomitant attenuation in the ANS fluorescence at 470 nm (36). The quality of these kinetic studies is illustrated in supplemental Fig. S2 by fitting sensorgrams recorded for the interaction with ATF.

SMB Binding to uPAR$^{H47C-N259C}$ Is Not Stimulated by uPA Occupancy—We have previously demonstrated that the affinity of the interaction between the SMB domain of vitronectin and uPAR^{wt} is increased ~4-fold upon receptor occupancy with GFD, ATF, or pro-uPA (17). To test if a similar uPA dependence in SMB binding also applies to uPAR$^{H47C-N259C}$, we immobi-

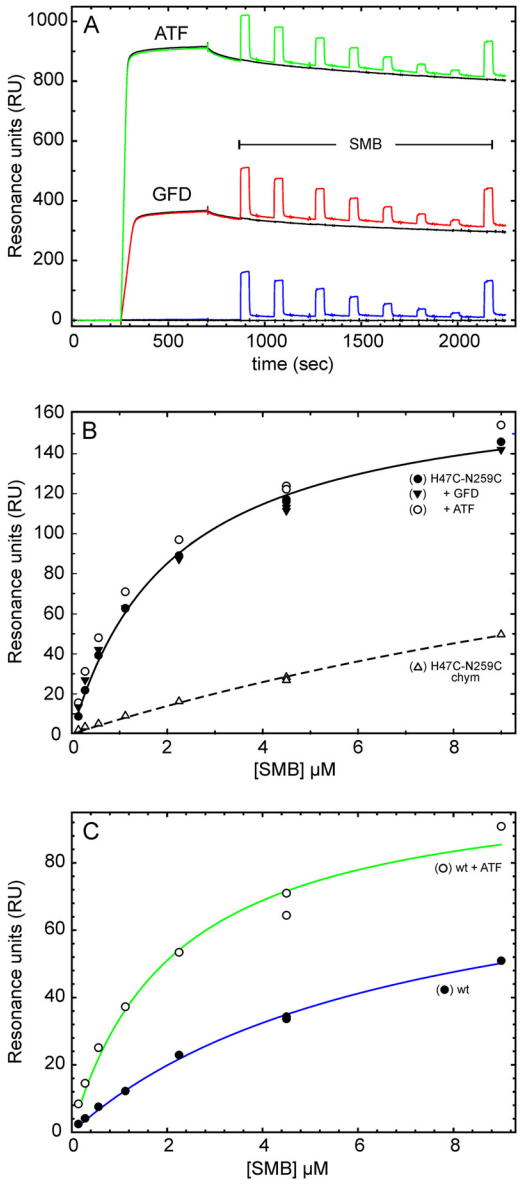

FIGURE 4. **SMB binding to uPAR$^{H47C-N259C}$.** *Panel A* shows the binding of a 2-fold dilution series of SMB (9 to 0.1 μM including repeat measurements at 4.5 μM) to immobilized uPAR$^{H47C-N259C}$ (2665 RU, ~76 fmol/mm^2) in its unoccupied state (*blue curve*) or after saturation by previous injections of 100 nM GFD (*red curve*) or ATF (*green curve*). The superimposed *black curves* represent equivalent binding curves, but omitting the injections of SMB. The derived equilibrium binding isotherms are shown in *panel B* for unoccupied uPAR$^{H47C-N259C}$ (●) and preformed complexes with GFD (▼) and ATF (○). Only the fit for unoccupied uPAR$^{H47C-N259C}$ is shown (*solid line*), as there were no significant differences after ligand saturation. The binding isotherm for uPAR$^{H47C-N259C/chym}$ is also shown (△) along with its fit (*dotted line*). For comparison, the corresponding binding isotherms are shown in *panel C* for unoccupied uPAR^{wt} (●) and its complex with ATF (○).

lized uPAR^{wt}, uPAR$^{H47C-N259C}$, and uPAR$^{H47C-N259C/chym}$ on a CM5 sensor chip and measured the equilibrium binding of SMB with and without previous receptor saturation with GFD or ATF. This experimental setup is illustrated in Fig. 4*A* for uPAR$^{H47C-N259C}$, where short pulses of 2-fold serial dilutions of purified SMB (starting at 9 μM) are allowed to interact with unoccupied receptor (*blue*) or receptors saturated with GFD (*red*) and ATF (*green*). The equilibrium dissociation constants (K_d) for these SMB interactions are subsequently determined by nonlinear curve fitting to the respective binding isotherms (Fig. 4, *B* and *C*). The stimulatory effect of occupying the hydrophobic ligand-binding cavity in uPAR^{wt} with receptor-binding derivatives of uPA is, reassuringly, recapitulated in this experimental setting, where the affinity for SMB binding is increased 3-fold after binding to GFD or ATF (Table 2). Notably, unoccupied uPAR$^{H47C-N259C}$ already adopts the moderately higher affinity state for SMB, which normally requires saturation by uPA, and no additional increase in this affinity is recorded on binding GFD or ATF. This suggests that the conformational constraint induced by the covalent cross-link between DI and DIII bypasses the regulatory role of uPA binding that is generally modulating the affinity for SMB (17). This raises the intriguing possibility that the conformational constraint introduced by the distant interdomain cross-link has rendered the receptor "constitutively active" with respect to vitronectin binding.

Although the chymotrypsin cleavage of the Tyr^{87}-Ser^{88} peptide bond situated in the linker region between DI and DII does not directly involve residues confined to the structural and functional epitope on uPAR for SMB binding (17, 22), this cleavage is, nonetheless, accompanied by a ~10-fold increase in the K_d for this interaction (Table 2). This impact on SMB binding is most likely caused by a local distortion of the adjacent SMB binding site, which could involve displacement of the hot spot residue Arg^{91}. Occupancy by ATF or GFD did not increase the affinity of uPAR$^{H47C-N259C/chym}$ for SMB (Table 2).

Lamellipodia-inducing Potential in HEK293 Cells Expressing uPAR$^{H47C-N259C}$—To measure the impact of locking uPAR in the closed conformation on its ability to induce lamellipodia in cells plated on vitronectin, we stably transfected HEK293 cells with 8 different uPAR mutants. These were designed to compare the constrained *versus* unconstrained states of uPAR, but they also harbor various additional mutations to superimpose a gradual impairment on their inherent vitronectin-binding properties (17). Based on our functional and structural data (17, 22), we thus introduced two mutations (W32A and R91D) in the vitronectin-binding interface of uPAR to obtain a differential attenuation of this interaction. All transfected HEK293 cell lines express comparable levels of both uPAR protein and functional high-affinity binding sites for uPA as assessed by ELISA and time-resolved fluorescence assay for uPA binding (supplemental Table S1 and Fig. S3). As reported previously (16, 18, 24), we find that HEK293 cells first acquire lamellipodia in response to exposure to vitronectin-coated surfaces when they are transfected with uPAR^{wt}. This ability is, however, not acquired if they are transfected with uPAR mutants having reduced affinity for vitronectin, *i.e.* uPAR^{W32A}, uPAR^{R91D}, or uPAR$^{W32A-R91D}$ (Fig. 5*A*). As noted previously, the functional deficiency of uPAR^{W32A} can, nevertheless, be restored by receptor occupancy with uPA or its minimal receptor-binding module GFD (16, 24). Further substantiating this finding, we now report that the level of rescue appears correlated to the severity of the impairment in vitronectin binding, *i.e.* with a decreasing efficacy from uPAR^{W32A} → uPAR^{R91D} → uPAR$^{W32A-R91D}$ (Fig. 5*B*). This relationship emphasizes the importance of the interplay between uPAR and vitronectin for lamellipodia formation under these experimental conditions.

TABLE 2
Equilibrium binding constants for SMB-uPAR$^{H47C\text{-}N259C}$ interactions

Immobilized reactant[a]	Preformed complex[b]	K_d (SMB)[c]	R_{max} (SMB)[d]	R_{max} (GFD or ATF)[e]
		10^{-6} M	fmol/mm^2	
uPAR^{wt}	None	7.0 ± 0.7	14.5 ± 0.9	
uPAR^{wt}	GFD	2.2 ± 0.4	17.1 ± 1.1	31.5
uPAR^{wt}	ATF	2.5 ± 0.3	15.9 ± 0.8	26.5
uPAR$^{H47C\text{-}N259C}$	None	2.1 ± 0.2	28.6 ± 0.8	
uPAR$^{H47C\text{-}N259C}$	GFD	1.6 ± 0.2	28.1 ± 1.1	67.7
uPAR$^{H47C\text{-}N259C}$	ATF	1.8 ± 0.2	26.5 ± 1.1	56.5
uPAR$^{H47C\text{-}N259C/chym}$	None	23 ± 6	28.6 ± 6.0	
uPAR$^{H47C\text{-}N259C/chym}$	GFD	16 ± 2	29.1 ± 2.6	77.8
uPAR$^{H47C\text{-}N259C/chym}$	ATF	18 ± 3	26.3 ± 3.4	63.7

[a] Relatively high levels of uPAR were immobilized by amine chemistry (5 μg/ml) in 3 consecutive flow cells of a CM5 sensor chip: uPAR^{wt} (2632 RU), uPAR$^{H47C\text{-}N259C}$ (2665 RU), and uPAR$^{H47C\text{-}N259C/chym}$ (2671 RU). These levels are equivalent to a surface density of approximately 76 fmol/mm^2.
[b] The indicated bimolecular complexes were formed by injecting 100 nM of the respective uPA derivatives for 450 s at 20 °C using a flow rate of 20 μl/min.
[c] Two-fold dilution series of purified SMB were consecutively injected at a flow rate of 20 μl/min at 20 °C covering the concentration range from 0.14 to 9 μM. No regeneration was needed due to the very fast dissociations rates. The equilibrium binding constants K_d and R_{max} for these weak interactions were calculated from the corresponding equilibrium binding isotherms by nonlinear curve fitting assuming saturation of a single binding site: $R_{eq} = (R_{max}(SMB))/(K_d + (SMB))$, where R_{eq} is the binding level at equilibrium, and R_{max} is the binding capacity of the chip.
[d] R_{max} values were calculated from the above fittings assuming that 1 RU ~ 1 pg/mm^2 and the average molecular mass of SMB is 6,154 Da.
[e] R_{max} values for the first interaction with the respective pro-uPA derivatives, which were injected at high concentration (100 nM), were measured directly from the recorded sensorgrams just before the first SMB injection (see Fig. 4*A*). The following average molecular masses were used for these calculations: GFD$^{1-48}$ (5,362 Da) and ATF$^{1-143}$ (16,189 Da).

Turning to the constrained uPAR$^{H47C\text{-}N259C}$, we now demonstrate that stabilizing the interface between DI and DIII via a covalent cross-link endows uPAR with a constitutive lamellipodia-inducing activity, which then circumvents the regulatory role of uPA binding (Fig. 5, compare *A* and *B versus C*). Importantly, HEK293 cells expressing uPAR$^{H47C\text{-}N259C/W32A}$ mount an uncompromised induction of lamellipodia on vitronectin (Fig. 5*C*), which is in clear contrast to the impaired responsiveness displayed by the correspondingly unconstrained uPAR^{W32A} (Fig. 5*A*). We have thus managed to create a molecular mimicry of the regulatory gain-of-function, which under normal conditions is elicited by receptor occupancy with uPA, as illustrated for uPAR^{W32A}-GFD complexes in Fig. 5*B*. The magnitude of the functional rescue obtained by the engineered disulfide parallels the potency of the GFD-bound receptor, as both partly restore the deficiency of uPAR^{R91D}, whereas neither can rescue the more severely compromised uPAR$^{W32A\text{-}R91D}$ (Fig. 5, *A–C*). The observed correlation between the lamellipodia-inducing efficacy of both uPAR^{wt}-GFD and uPAR$^{H47C\text{-}N259C}$ with the severity of the mutational impact on vitronectin binding thus further emphasizes the importance of this interaction for both receptors.

We have previously shown that several monoclonal anti-uPAR antibodies having their epitopes located in DI close to the interdomain interface with DIII (epitope bin 2, *e.g.* mAbs R5, R9, and mR1) inhibit the ability of uPAR to stimulate lamellipodia formation (24). This effect is presumably instigated by trapping an *open* uPAR conformation incapable of promoting lamellipodia formation. In the present study, we have now mapped the functional epitope for an additional anti-uPAR mAb designated H2, which effectively inhibits uPA and vitronectin binding, and in so doing attenuates, *e.g.* angiogenesis (39). As illustrated in Fig. 6*A*, the dominating hot spot for H2 is Asn^{259} in uPAR DIII, which is one of two anchoring sites for the covalent cross-link introduced in uPAR$^{H47C\text{-}N259C}$. In the crystal structure of uPAR-ATF complexes, Asn^{259} is repositioned more than 10 Å within the domain interface of DI and DIII compared with the corresponding uPAR-peptide antagonist complex (Fig. 6*A*). We therefore investigated the impact of H2 as well as previously characterized anti-uPAR mAbs representing epitope bins 1 and 2 (24) on lamellipodia formation in HEK293 cells transfected with uPAR^{wt} and uPAR$^{H47C\text{-}N259C}$.

As shown in Fig. 6*B*, anti-uPAR mAbs belonging to epitope bins 1 and 2 in uPAR DI all inhibit lamellipodia formation in HEK293 cells expressing uPAR^{wt} (24), as does the newly characterized mAb H2. Remarkably, none of these mAbs inhibit the lamellipodia induced by uPAR$^{H47C\text{-}N259C}$. The topographic location of these epitope bins in the uPAR-ATF complex are illustrated in Fig. 6*C*, emphasizing the pairwise proximity of epitope bin 1 to the SMB binding site and epitope bin 2 to the engineered cross-linking site. The resilience of lamellipodia in uPAR$^{H47C\text{-}N259C}$-transfected HEK293 cells to inhibition by H2 and mAbs from epitope bin 2 may thus be anticipated due to the proximity of their epitopes to the introduced interdomain cross-link. To our surprise, mAbs recognizing epitope bin 1 are, however, also incapable of preventing lamellipodia formation in the uPAR$^{H47C\text{-}N259C}$-transfected HEK293 cells, despite their epitopes being located adjacent to the vitronectin binding site and distant to the introduced disulfide (Fig. 6*C*). This conundrum is most likely related to the same allosteric changes that increase the affinity for SMB in uPAR$^{H47C\text{-}N259C}$. We thus hypothesize that although these changes are beneficial for the formation of an optimal SMB binding site, they do, nevertheless, distort epitopes recognized by mAbs belonging to bin 1. This proposition is further substantiated experimentally by the reduced affinities of these mAbs toward uPAR$^{H47C\text{-}N259C}$ compared with uPAR^{wt} as measured by surface plasmon resonance. The predominant effect, which we observe primarily on the k_{on} values, argues for a suboptimal spatial arrangement of these epitopes, which slows down the formation of a productive bimolecular encounter complex (Table 3).

DISCUSSION

With the advent of a steadily growing number of experimentally determined crystal structures for uPAR in complex with various natural and synthetic ligands (5, 21, 22, 25), our perception of the structural basis underlying uPAR function is becoming progressively more coherent (13). In recent years, it has

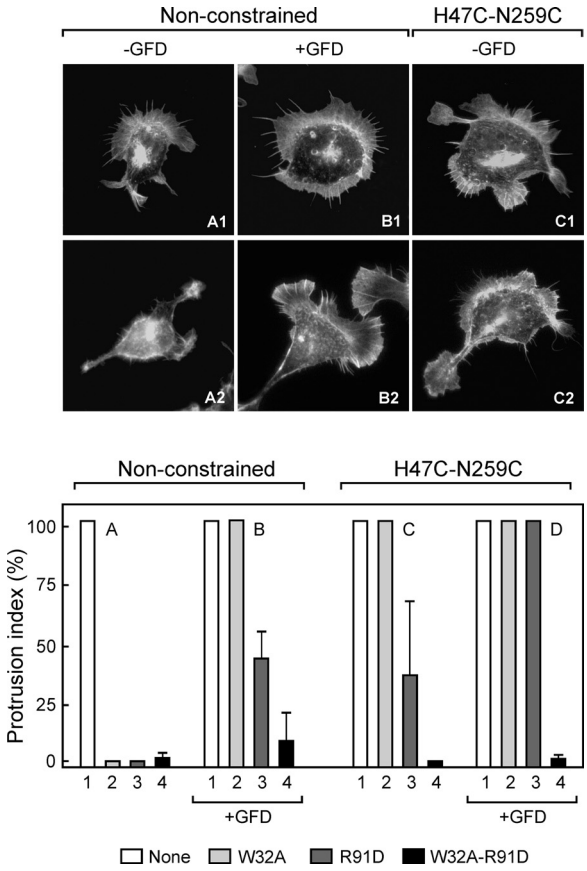

FIGURE 5. **Glycolipid-anchored uPAR$^{H47C-N259C}$ in HEK293 cells mimics GFD-bound uPAR^{wt} in the induction of lamellipodia.** The ability to form lamellipodia on vitronectin-coated surfaces was measured for HEK293 cells after stable transfection with 8 different uPAR constructs. Representative micrographs are shown in the *upper panels* for uPAR^{wt} (*A1* and *B1*), uPAR^{W32A} (*A2* and *B2*), uPAR$^{H47C-N259C}$ (*C1*), and uPAR$^{H47C-N259C/W32A}$ (*C2*). A graphic representation summarizing the results is provided in the *lower panel*. Nonconstrained uPAR^{wt} (*lane 1*) and mutants with impaired vitronectin binding properties, *i.e.* uPAR^{W32A} (*lane 2*), uPAR^{R91D} (*lane 3*), and uPAR$^{W32A-R91D}$ (*lane 4*), were probed in their unoccupied state in *cluster A*. The impact of uPA ligation is probed in *cluster B* for the same set of transfected HEK293 cells by incubation with 100 nM GFD during cell seeding and incubation on vitronectin. The impact of locking uPAR in the closed conformation *per se* is tested in *cluster C* for HEK293 cells transfected with uPAR$^{H47C-N259C}$ (*lane 1*) combined with the same mutations as in cluster A, *i.e.* uPAR$^{H47C-N259C/W32A}$ (*lane 2*), uPAR$^{H47C-N259C/R91D}$ (*lane 3*), and uPAR$^{H47C-N259C/W32A-R91D}$ (*lane 4*). The impact of GFD saturation is measured for these constrained uPAR mutants in *cluster D*.

become increasingly clear that the so-called "nonproteolytic role" of uPAR in cell adhesion and migration in many cases is tightly controlled by uPA occupancy (17, 18, 40). Although many reports on uPAR-vitronectin-mediated cell adhesion and migration employ transfected cell lines expressing high levels of uPAR (16, 18, 24, 41, 42), the regulatory role of uPA occupancy is, nevertheless, allegedly more noticeable in cells either expressing moderate to low levels of uPAR (40, 43, 44) or alternatively, as in this study, in cells expressing high levels of uPAR mutants with an attenuated vitronectin binding. The proposition of such a regulatory role of uPA binding is quite conceivable from a physiological point of view, taking into consideration that its affinity for uPAR ($K_d \sim 0.5$ nM) nicely complements the levels of pro-uPA present under normal homeostatic conditions, *i.e.* 20 pM in plasma (45), thus setting the stage for an efficient responsiveness to increased local concentrations of pro-uPA. We have launched a new molecular model for the structure-function relationships in the uPA-uPAR interaction, which emphasizes the importance of the conformational flexibility in the modular assembly of uPAR (24). Importantly, this model enables uPA occupancy *per se* to act as the driving force for the allosteric regulation of uPAR-assisted lamellipodia formation, as is observed in HEK293 cells (summarized in Fig. 7). One of the important ramifications of this model is the prediction that in theory, it should be possible to engineer a constitutively active uPAR by stabilizing the closed conformation of uPAR. In the present study, we have verified this prediction experimentally by introducing a covalent cross-link (disulfide bond) between DI (position 47) and DIII (position 259). The remarkable efficacy in oxidation of the introduced pair of non-natural cysteines yields a homogenous ensemble of uPAR molecules with a uniform interdomain tethering under normal expression conditions, which renders this mutant optimally suited for studies both *in vitro* and *in vivo*.

The restricted conformational space explored by our constrained uPAR$^{H47C-N259C}$ mutant does at first sight not affect the real-time binding kinetics for uPA. Scrutinizing the thermodynamic parameters of the uPA-uPAR interaction reveals, nevertheless, different contributions from enthalpy and entropy (supplemental Fig. S1). Although some precaution should always be exercised when translating thermodynamic properties into simplified structural models, it is tempting to suggest that this difference pertains to the preassembly of an active hydrophobic ligand-binding cavity in the uPAR$^{H47C-N259C}$ mutant.

Another relevant observation is the finding that enzymatic cleavage in the linker region between DI and DII in uPAR$^{H47C-N259C}$ does not reduce uPA binding as is the case for uPAR^{wt}. It should therefore be interesting to test how this interdomain stabilization affects functions proposed to be regulated by the cleavage of the linker region in uPAR^{wt}, *e.g.* FPR like-1 receptor-mediated chemotaxis (28, 46) or LRP-mediated internalization (27).

The present demonstration of functional mimicry of the vitronectin binding properties of uPA-uPAR complexes by uPAR$^{H47C-N259C}$ has wide implications for our understanding of the regulatory mechanisms for uPAR-assisted lamellipodia formation in cells responding to matrix-embedded vitronectin. In cases where uPA-independent functions of uPAR are reported in genetic studies, *e.g.* in the development of focal segmental glomerulosclerosis (47, 48), it is reasonable to consider the *open* form of uPAR as a putative causative agent. In other cases, however, where uPA-dependent functions of uPAR are reported to be independent of plasminogen activation, *e.g.* in motor neuron remodeling (49) or in adhesion and migration on vitronectin (17, 18, 40), it is reasonable to consider the *closed* form of uPAR as the active substance. Being an almost perfect surrogate for the "nonproteolytic functions" elicited by the bimolecular uPA-uPAR complexes in adhesion on vitronectin, our uPAR$^{H47C-N259C}$ mutant can thus conveniently be used as a stable, mono-component bait in ligand experiments to isolate potential interaction partners involved in the latter processes. A particularly elegant genetic setup to further challenge the nonproteolytic functions of uPA-uPAR complexes *in vivo*

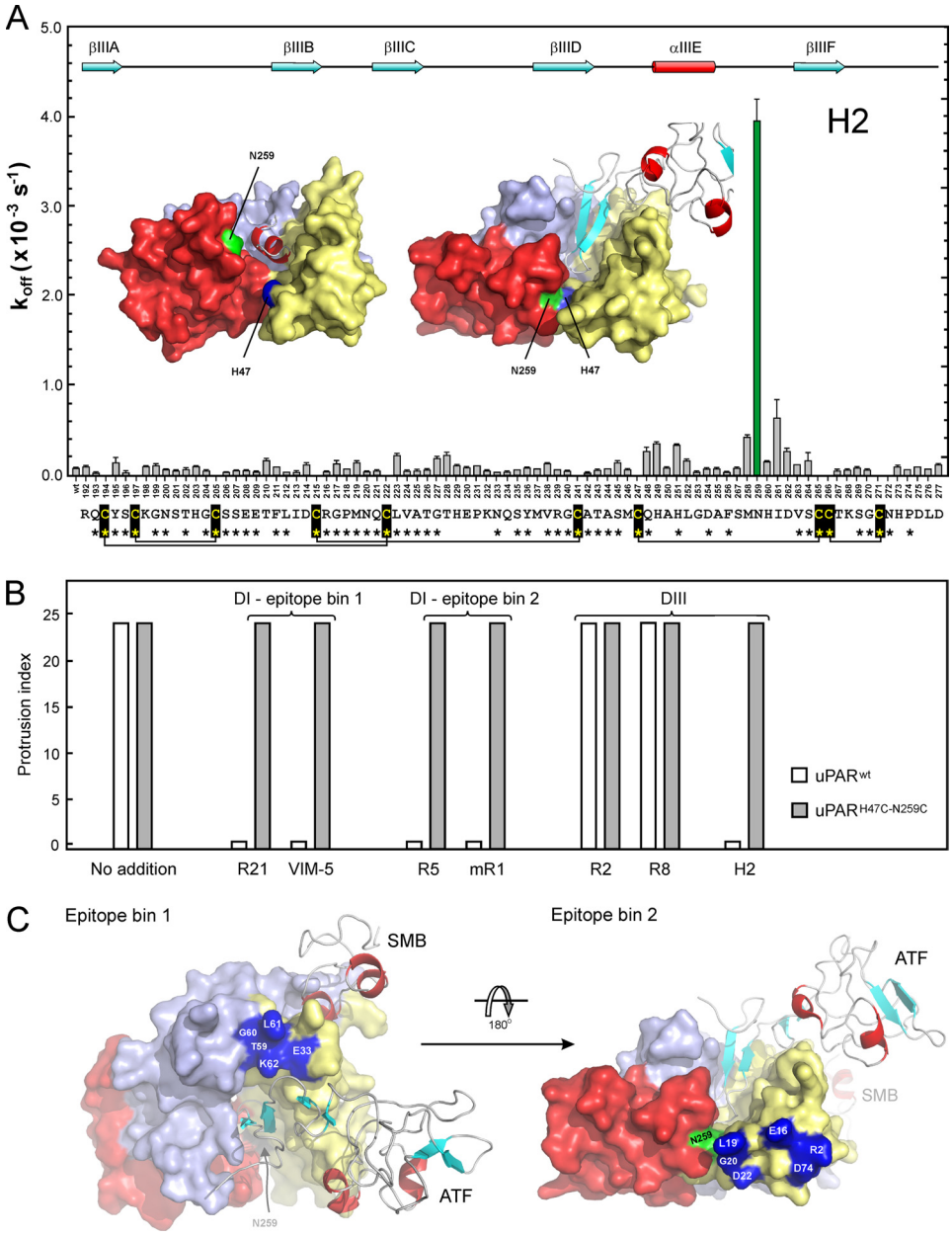

FIGURE 6. **Several anti-uPAR mAbs targeting domain interfaces abrogate lamellipodia in uPAR^{wt}, but not in uPAR$^{H47C-N259C}$-expressing HEK293 cells.** The location of the dominating hot spot for mAb H2 in intact uPAR$^{1-283}$ is illustrated in *panel A*. The interaction between immobilized mAb H2 and a serial 2-fold dilution series of purified human recombinant uPAR mutants (range 6–200 nM) was measured by surface plasmon resonance. The determined dissociation rate constants (k_{off}) are shown ($n = 6$) as a function of the positions in the primary sequence of human uPAR DIII$^{192-277}$ that were individually mutated to alanine (omitting positions occupied by cysteines). Secondary structure elements of uPAR DIII are shown in the *upper section* following a previously established nomenclature (25), whereas the primary sequence of DIII is shown at the *bottom* along with the disulfide connectivity and the sequence conservation relative to mouse uPAR (*asterisks* represent identical residues). Two *molecular models* are shown to visualize the locations of His^{47} in DI (*blue*) and Asn^{259} in DIII (*green*) in the crystal structures solved for uPAR in complex with a peptide antagonist (*left*) and the amino-terminal fragment of uPA (*right*). The bound peptide antagonist or ATF are both shown as ribbon diagrams, whereas uPAR is shown in a surface representation with DI, DII, and DIII colored *yellow*, *light blue*, and *red*. The impact of various anti-uPAR mAbs on lamellipodia formation in HEK293 cells transfected with either uPAR^{wt} (*open bars*) or uPAR$^{H47C-N259C}$ (*filled bars*) are shown in *panel B*. An overview of the topographic location of epitope bins 1 and 2 (*blue*) relative to the introduced disulfide constraint (His^{47} and Asn^{259} in *green*) and the SMB binding site is illustrated in *panel C* using PDB 3BT1 coordinates for the ternary ATF-uPAR-SMB complex.

would be to replace the *Plaur* gene with one encoding an equivalently constrained mouse uPAR and test this transgenic mouse strain after crossing it into a uPA$^{-/-}$ background.

In future attempts to develop selective inhibitors targeting active uPAR, the stable conformation of the constrained uPAR$^{H47C-N259C}$ may also be superior: 1) as bait in drug screening programs using fragment-based or small molecule libraries, or 2) as an antigen for developing mAbs recognizing this particularly active conformation of uPAR. As a first challenge, we have used this mutant to successfully solve the first crystal structure of an unoccupied uPAR,[3] which has proven elusive for many years. In line with the ANS data reported here, this structure reveals that the stabilized unoccupied uPAR$^{H47C-N259C}$ manages to assemble a *bona fide*

TABLE 3
Kinetics for mAbs interacting with uPAR^{wt} and uPAR$^{H47C\text{-}N259C}$

Immobilized mAb[a]	Analyte[b]	k_{on}[c]	k_{off}[c]	K_d[c]	Ratio (k_{on}), uPAR$^{H57C\text{-}N259}$/uPAR^{wt}
		$10^5\ M^{-1}s^{-1}$	$10^{-4}\ s^{-1}$	$10^{-9}\ M$	
R21	uPAR^{wt}	4.0 ± 2.3	4.7 ± 1.4	1.2	
R21	uPAR$^{H47C\text{-}N259C}$	**0.1 ± 0.0**	3.9 ± 0.3	39	**0.03**
VIM-5	uPAR^{wt}	1.9 ± 0.5	16.1 ± 0.8	8.5	
VIM-5	uPAR$^{H47C\text{-}N259C}$	**0.3 ± 0.2**	14.5 ± 1.0	48	**0.16**
R5	uPAR^{wt}	3.6 ± 0.6	10.8 ± 0.4	3.0	
R5	uPAR$^{H47C\text{-}N259C}$	**0.9 ± 0.5**	13.6 ± 0.8	15	**0.25**
mR1	uPAR^{wt}	1.6 ± 0.5	1.0 ± 0.3	0.63	
mR1	uPAR$^{H47C\text{-}N259C}$	**0.1 ± 0.0**	31.1 ± 1.2	258	**0.06**
R8	uPAR^{wt}	6.8 ± 2.5	1.8 ± 0.6	0.26	
R8	uPAR$^{H47C\text{-}N259C}$	12.8 ± 4.5	3.5 ± 0.6	0.25	1.9
R2	uPAR^{wt}	3.5 ± 1.0	0.7 ± 0.2	0.20	
R2	uPAR$^{H47C\text{-}N259C}$	2.4 ± 1.0	1.0 ± 0.5	0.41	0.69
R24	uPAR^{wt}	6.7 ± 1.9	6.1 ± 0.1	0.91	
R24	uPAR$^{H47C\text{-}N259C}$	10.7 ± 3.2	5.3 ± 0.1	0.49	1.6
H2	uPAR^{wt}	1.3 ± 0.4	0.3 ± 0.1	0.25	
H2	uPAR$^{H47C\text{-}N259C}$	NB[d]	NB	NB	NB

[a] Low levels of anti-uPAR mAbs were immobilized by amine chemistry on the CM5 sensor chip. The tested mAbs are grouped according to their epitope locations: *DI bin 1* (R21 and VIM-5), *DI bin 2* (R5 and mR1), DIIDIII (R8), and DIII (R2, R24, and H2).
[b] Two-fold dilution series of ligands were measured at 20 °C at a flow rate of 50 μl/min covering the concentration range from 0.1 to 50 nM. Long dissociation phases (20 min) were included due to the tight binding of some of these mAbs.
[c] The kinetic rate constants for the interaction between immobilized anti-uPAR mAbs and the purified uPAR^{wt} and uPAR$^{H47C\text{-}N259C}$ were measured as specified under "Materials and Methods."
[d] NB, no binding detected.

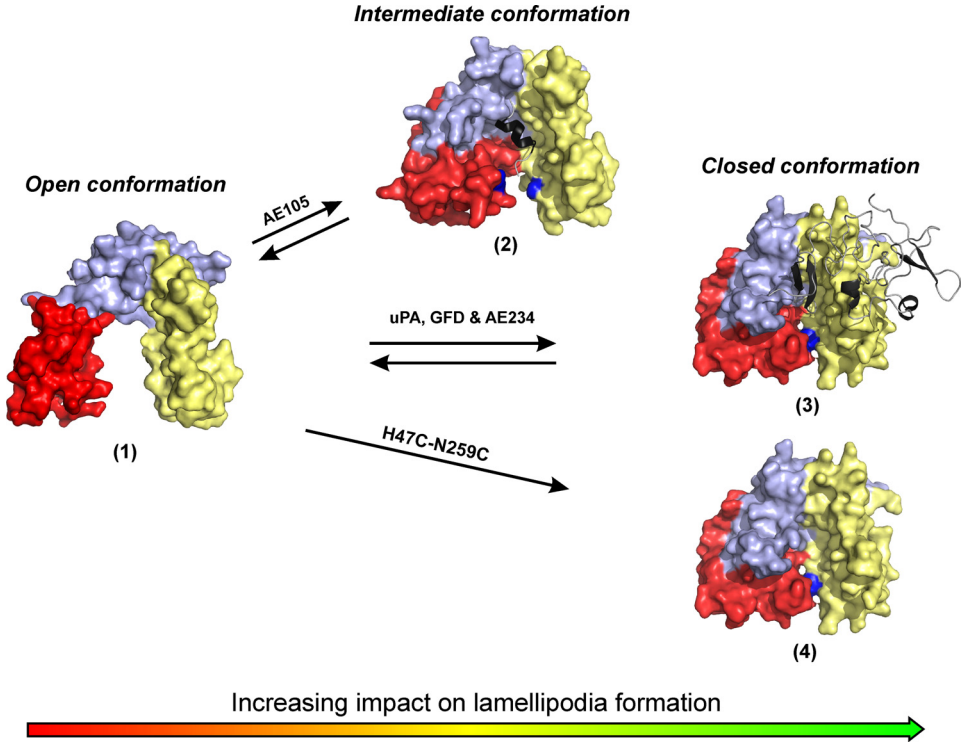

FIGURE 7. **Mimicry of the allosteric role of uPA binding on uPAR-dependent lamellipodia formation.** The three homologous LU domains in uPAR (colored *yellow*, *light blue*, and *red*) are separated by relatively long linker regions, and we propose (24) that a considerable inherent conformational flexibility exists in this multidomain assembly. The *open* conformation of unoccupied uPAR (*1*), which is inferred from our biochemical data, is a poor "cofactor" for induction of lamellipodia on vitronectin-rich matrices. Engagement of the hydrophobic ligand-binding cavity by AE105 (*2*) or uPA (*3*) drives the uPAR conformation towards an *intermediate* and *closed* state, respectively, the structures of which are confirmed by x-ray crystallography (PDB codes 1YWH and 2FD6). A covalent cross-link between domains I and III introduced by genetic engineering (uPAR$^{H47C\text{-}N259C}$) traps uPAR in the closed conformation and generates a constitutively active receptor independent of uPA binding (*4*). This structure has recently been confirmed by x-ray crystallography.[3]

large, but basically empty, hydrophobic ligand-binding cavity, despite its exposure to the solvent (26). It should, nonetheless, be emphasized that this structure represents the *closed* conformation of uPAR and that the structure of the unoccupied *open* conformation of uPAR still remains to be solved. We are currently attempting to define the conformational space explored by unoccupied uPAR^{wt} using small angle x-ray scattering (50).

Acknowledgments—We thank Gitte Juhl Funch, Haldis Egholm Mønsted, and John Post for excellent technical assistance.

REFERENCES

1. Ploug, M., Rønne, E., Behrendt, N., Jensen, A. L., Blasi, F., and Danø, K. (1991) *J. Biol. Chem.* **266,** 1926–1933
2. Liu, S., Bugge, T. H., and Leppla, S. H. (2001) *J. Biol. Chem.* **276,** 17976–17984
3. Liu, S., Aaronson, H., Mitola, D. J., Leppla, S. H., and Bugge, T. H. (2003) *Proc. Natl. Acad. Sci. U.S.A.* **100,** 657–662
4. Pass, J., Jögi, A., Lund, I. K., Rønø, B., Rasch, M. G., Gårdsvoll, H., Lund, L. R., Ploug, M., Rømer, J., Danø, K., and Høyer-Hansen, G. (2007) *Thromb. Haemost.* **97,** 1013–1022
5. Lin, L., Gårdsvoll, H., Huai, Q., Huang, M., and Ploug, M. (2010) *J. Biol. Chem.* **285,** 10982–10992
6. Connolly, B. M., Choi, E. Y., Gårdsvoll, H., Bey, A. L., Currie, B. M., Chavakis, T., Liu, S., Molinolo, A., Ploug, M., Leppla, S. H., and Bugge, T. H. (2010) *Blood* **116,** 1593–1603
7. Pyke, C., Kristensen, P., Ralfkiaer, E., Grøndahl-Hansen, J., Eriksen, J., Blasi, F., and Danø, K. (1991) *Am. J. Pathol.* **138,** 1059–1067
8. Nielsen, B. S., Rank, F., Illemann, M., Lund, L. R., and Danø, K. (2007) *Int. J. Cancer* **120,** 2086–2095
9. Hildenbrand, R., Niedergethmann, M., Marx, A., Belharazem, D., Allgayer, H., Schleger, C., and Ströbel, P. (2009) *Am. J. Pathol.* **174,** 2246–2253
10. Foekens, J. A., Peters, H. A., Look, M. P., Portengen, H., Schmitt, M., Kramer, M. D., Brünner, N., Jänicke, F., Meijer-van Gelder, M. E., Henzen-Logmans, S. C., van Putten, W. L., and Klijn, J. G. (2000) *Cancer Res.* **60,** 636–643
11. Stephens, R. W., Nielsen, H. J., Christensen, I. J., Thorlacius-Ussing, O., Sørensen, S., Danø, K., and Brünner, N. (1999) *J. Natl. Cancer Inst.* **91,** 869–874
12. Ngo, J., Jiang, L., Lin, Z., Yuan, C., Chen, Z., Zhang, X., Yu, H., Wang, J., Lin, L., and Huang, M. (2011) *Curr. Drug Targets* **12,** 1729–1743
13. Kriegbaum, M. C., Persson, M., Haldager, L., Alpizar-Alpizar, W., Jacobsen, B., Gårdsvoll, H., Kjaer, A., and Ploug, M. (2011) *Curr. Drug Targets* **12,** 1711–1728
14. Wei, Y., Czekay, R. P., Robillard, L., Kugler, M. C., Zhang, F., Kim, K. K., Xiong, J. P., Humphries, M. J., and Chapman, H. A. (2005) *J. Cell Biol.* **168,** 501–511
15. Wei, Y., Lukashev, M., Simon, D. I., Bodary, S. C., Rosenberg, S., Doyle, M. V., and Chapman, H. A. (1996) *Science* **273,** 1551–1555
16. Hillig, T., Engelholm, L. H., Ingvarsen, S., Madsen, D. H., Gårdsvoll, H., Larsen, J. K., Ploug, M., Danø, K., Kjøller, L., and Behrendt, N. (2008) *J. Biol. Chem.* **283,** 15217–15223
17. Gårdsvoll, H., and Ploug, M. (2007) *J. Biol. Chem.* **282,** 13561–13572
18. Madsen, C. D., Ferraris, G. M., Andolfo, A., Cunningham, O., and Sidenius, N. (2007) *J. Cell Biol.* **177,** 927–939
19. Gårdsvoll, H., Gilquin, B., Le Du, M. H., Ménèz, A., Jørgensen, T. J., and Ploug, M. (2006) *J. Biol. Chem.* **281,** 19260–19272
20. Deng, G., Curriden, S. A., Wang, S., Rosenberg, S., and Loskutoff, D. J. (1996) *J. Cell Biol.* **134,** 1563–1571
21. Huai, Q., Mazar, A. P., Kuo, A., Parry, G. C., Shaw, D. E., Callahan, J., Li, Y., Yuan, C., Bian, C., Chen, L., Furie, B., Furie, B. C., Cines, D. B., and Huang, M. (2006) *Science* **311,** 656–659
22. Huai, Q., Zhou, A., Lin, L., Mazar, A. P., Parry, G. C., Callahan, J., Shaw, D. E., Furie, B., Furie, B. C., and Huang, M. (2008) *Nat. Struct. Mol. Biol.* **15,** 422–423
23. Kjaergaard, M., Hansen, L. V., Jacobsen, B., Gårdsvoll, H., and Ploug, M. (2008) *Front. Biosci.* **13,** 5441–5461
24. Gårdsvoll, H., Jacobsen, B., Kriegbaum, M. C., Behrendt, N., Engelholm, L., Østergaard, S., and Ploug, M. (2011) *J. Biol. Chem.* **286,** 33544–33556
25. Llinas, P., Le Du, M. H., Gårdsvoll, H., Danø, K., Ploug, M., Gilquin, B., Stura, E. A., and Ménez, A. (2005) *EMBO J.* **24,** 1655–1663
26. Behrendt, N., Ploug, M., Patthy, L., Houen, G., Blasi, F., and Danø, K. (1991) *J. Biol. Chem.* **266,** 7842–7847
27. Nieves, E. C., and Manchanda, N. (2010) *J. Biol. Chem.* **285,** 12595–12603
28. Mazzieri, R., D'Alessio, S., Kenmoe, R. K., Ossowski, L., and Blasi, F. (2006) *Mol. Biol. Cell* **17,** 367–378
29. Bernstein, A. M., Twining, S. S., Warejcka, D. J., Tall, E., and Masur, S. K. (2007) *Mol. Biol. Cell* **18,** 2716–2727
30. Stratton-Thomas, J. R., Min, H. Y., Kaufman, S. E., Chiu, C. Y., Mullenbach, G. T., and Rosenberg, S. (1995) *Protein Eng.* **8,** 463–470
31. Kjaergaard, M., Gårdsvoll, H., Hirschberg, D., Nielbo, S., Mayasundari, A., Peterson, C. B., Jansson, A., Jørgensen, T. J., Poulsen, F. M., and Ploug, M. (2007) *Protein Sci.* **16,** 1934–1945
32. Gårdsvoll, H., Werner, F., Søndergaard, L., Danø, K., and Ploug, M. (2004) *Protein Expr. Purif.* **34,** 284–295
33. Jacobsen, B., Gårdsvoll, H., Juhl Funch, G., Ostergaard, S., Barkholt, V., and Ploug, M. (2007) *Protein Expr. Purif.* **52,** 286–296
34. Ploug, M., Kjalke, M., Rønne, E., Weidle, U., Høyer-Hansen, G., and Danø, K. (1993) *J. Biol. Chem.* **268,** 17539–17546
35. Riisbro, R., Christensen, I. J., Piironen, T., Greenall, M., Larsen, B., Stephens, R. W., Han, C., Høyer-Hansen, G., Smith, K., Brünner, N., and Harris, A. L. (2002) *Clin. Cancer Res.* **8,** 1132–1141
36. Ploug, M., Ellis, V., and Danø, K. (1994) *Biochemistry* **33,** 8991–8997
37. Petersen, M. T., Jonson, P. H., and Petersen, S. B. (1999) *Protein Eng.* **12,** 535–548
38. Teilum, K., Olsen, J. G., and Kragelund, B. B. (2009) *Cell. Mol. Life Sci.* **66,** 2231–2247
39. Kroon, M., Koolwijk, P., van Goor, H., Weidle, U. H., Collen, A., van der Pluijm, G., and van Hinsbergh, V. W. (1999) *Am. J. Pathol.* **154,** 1731–1742
40. Waltz, D. A., and Chapman, H. A. (1994) *J. Biol. Chem.* **269,** 14746–14750
41. Jo, M., Lester, R. D., Montel, V., Eastman, B., Takimoto, S., and Gonias, S. L. (2009) *J. Biol. Chem.* **284,** 22825–22833
42. Kjøller, L., and Hall, A. (2001) *J. Cell Biol.* **152,** 1145–1157
43. Sidenius, N., and Blasi, F. (2000) *FEBS Lett.* **470,** 40–46
44. Waltz, D. A., Sailor, L. Z., and Chapman, H. A. (1993) *J. Clin. Invest.* **91,** 1541–1552
45. Grøndahl-Hansen, J., Agerlin, N., Munkholm-Larsen, P., Bach, F., Nielsen, L. S., Dombernowsky, P., and Danø, K. (1988) *J. Lab. Clin. Med.* **111,** 42–51
46. Resnati, M., Pallavicini, I., Wang, J. M., Oppenheim, J., Serhan, C. N., Romano, M., and Blasi, F. (2002) *Proc. Natl. Acad. Sci. U.S.A.* **99,** 1359–1364
47. Wei, C., Möller, C. C., Altintas, M. M., Li, J., Schwarz, K., Zacchigna, S., Xie, L., Henger, A., Schmid, H., Rastaldi, M. P., Cowan, P., Kretzler, M., Parrilla, R., Bendayan, M., Gupta, V., Nikolic, B., Kalluri, R., Carmeliet, P., Mundel, P., and Reiser, J. (2008) *Nat. Med.* **14,** 55–63
48. Wei, C., El Hindi, S., Li, J., Fornoni, A., Goes, N., Sageshima, J., Maiguel, D., Karumanchi, S. A., Yap, H. K., Saleem, M., Zhang, Q., Nikolic, B., Chaudhuri, A., Daftarian, P., Salido, E., Torres, A., Salifu, M., Sarwal, M. M., Schaefer, F., Morath, C., Schwenger, V., Zeier, M., Gupta, V., Roth, D., Rastaldi, M. P., Burke, G., Ruiz, P., and Reiser, J. (2011) *Nat. Med.* **17,** 952–960
49. Seeds, N., Mikesell, S., Vest, R., Bugge, T., Schaller, K., and Minor, K. (2011) *Cell. Mol. Neurobiol.* **31,** 961–967
50. Mertens, H. D., and Svergun, D. I. (2010) *J. Struct. Biol.* **172,** 128–141